Erschienen in: Nature Physics ; 16 (2020), 3. - S. 341-345. - Springer Science and Business Media
https://dx.doi.org/10.1038/s41567-019-0745-8

Sub-femtosecond electron transport in a nanoscale gap

Markus Ludwig[1], Garikoitz Aguirregabiria[2], Felix Ritzkowsky[1], Tobias Rybka[1], Dana Codruta Marinica[3], Javier Aizpurua[2], Andrei G. Borisov[3], Alfred Leitenstorfer[1] and Daniele Brida[1,4]*

The strong fields associated with few-cycle pulses can drive highly nonlinear phenomena, allowing the direct control of electrons in condensed matter systems. In this context, by employing near-infrared single-cycle pulse pairs, we measure interferometric autocorrelations of the ultrafast currents induced by optical field emission at the nanogap of a single plasmonic nanocircuit. The dynamics of this ultrafast electron nanotransport depends on the precise temporal field profile of the optical driving pulse. Current autocorrelations are acquired with sub-femtosecond temporal resolution as a function of both pulse delay and absolute carrier-envelope phase. Quantitative modelling of the experiments enables us to monitor the spatiotemporal evolution of the electron density and currents induced in the system and to elucidate the physics underlying the electron transfer driven by strong optical fields in plasmonic gaps. Specifically, we clarify the interplay between the carrier-envelope phase of the driving pulse, plasmonic resonance and quiver motion.

Femtosecond pulses consisting of only a few cycles of the optical carrier wave[1] have enabled breakthrough opportunities for the direct manipulation of electrons in condensed matter based on nonlinear phenomena as well as in free space via linear acceleration[2–18]. The traditional conditions for such control experiments required extreme pulse intensities at low repetition rates, imposing substantial difficulties for the extraction of the dynamics of individual charge carriers. Recently, several works paradigmatically changed the approach to exploit optical phenomena driven by strong fields by employing pulses with minute energy content at high repetition rates, thus allowing for the generation and manipulation of photoelectrons in nanoscale systems[4,19,20].

In this context, single-cycle pulses with an energy of only a few picojoules may result in extremely nonlinear optical phenomena within a few-nanometre gap between the tips of an optical antenna[19,21–25]. The strong electrical bias provided by the field contained in the ultrashort optical pulses has been harnessed to drive tunnelling and ballistic acceleration of electrons generating a current with PHz bandwidth[19,26]. This non-perturbative process is fully coherent with the driving radiation and occurs within a half-cycle of the near-infrared carrier wavelength[19]. Here, by performing interferomeric autocorrelation measurements with two identical replicas of single-cycle driving pulses, we directly access the attosecond dynamics of the optical field emission and electron transport in plasmonic gaps. Controllable variation of the carrier-envelope phase (CEP) of the pulses enriches the experimental acquisition of the interferometric traces by an additional variable that allows for a deep understanding and complete insight into the relationship between the photo-emitted electrons and the accelerating field. Time-dependent density functional theory (TDDFT) calculations of the optical field emission and subsequent acceleration of the electrons in the plasmonic gap accurately reproduce the experimental results. In this way, we elucidate the underlying microscopic phenomena, including visualization of the evolution of electron currents in time and space as a function of the CEP of the driving pulses.

Figure 1a depicts the conceptual scheme of the experiment. The single-cycle pulses are set at a variable delay Δt by a broadband dispersion-balanced Mach–Zehnder interferometer and then focused tightly onto the nanocircuit containing a single plasmonic bowtie antenna. The Au nanoantenna features a 6 nm open junction and was fabricated via electron-beam lithography (inset, Fig. 1a). Under a static electric bias, this structure exhibits a tunnelling-like current–voltage (I–V) characteristic that is antisymmetric and highly nonlinear[19]. The bowtie design allows for a sub-wavelength concentration of the electric field of the laser pulse into the gap, while at the same time preserving its single-cycle character owing to strong radiation damping[25].

A custom-designed Er:fibre laser system[1,27] operating at a repetition rate of 80 MHz generates 4.2 fs pulses from a tailored supercontinuum spanning from 800 nm to 2,200 nm generated in a highly nonlinear germanosilicate fibre. After compression, the optical transients have a full-width at half-maximum (FWHM) duration that corresponds to a single cycle of the carrier wavelength at 1,250 nm. Such single-cycle pulses are ideal for driving ultrafast transport experiments that exploit a non-perturbative phenomenon such as optical field emission[19]. The temporal profile of the pulses is characterized in Fig. 1b. A passive phase-locking scheme[28] is implemented in a way that allows arbitrary control of the CEP without affecting the temporal duration of the pulse[19]. These optical transients provide a strong and ultrafast bias for direct and coherent driving of electronic transport across the junction. Due to the strong nonlinearity of the optical field emission process, an optically induced symmetry break occurs in the electric transport, which leads to a net current that depends on the CEP of the driving pulse. Consequently, when sweeping the CEP over a range of 2π, the integral current passes through a maximum, crosses zero and finally completely reverses its direction.

[1]Department of Physics and Center for Applied Photonics, University of Konstanz, Konstanz, Germany. [2]Centro de Física de Materiales, Centro Mixto CSIC-UPV/EHU and Donostia International Physics Center (DIPC), Donostia–San Sebastián, Spain. [3]Institut des Sciences Moléculaires d'Orsay – UMR 8214, CNRS–Université Paris Sud, Orsay, France. [4]Physics and Materials Science Research Unit, University of Luxembourg, Luxembourg, Luxembourg.
*e-mail: daniele.brida@uni.lu

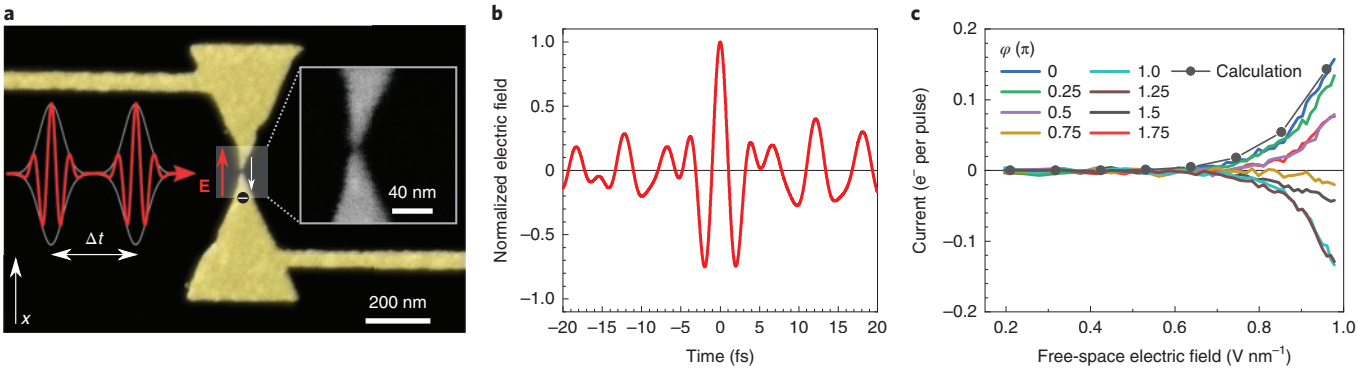

Fig. 1 | Driving ultrafast currents in a nanocircuit with single-cycle near-infrared pulses. a, Conceptual sketch of the experiment with two single-cycle light pulses delayed by a time Δt and focused on the nanocircuit. The relative CEP of the biasing pulses can be fully controlled with a precision of 10 mrad. Behind the sketch is a scanning electron micrograph (SEM) of the Au optical antenna with electrical leads on a fused-silica substrate, as well as an enlarged view into the gap region (inset). The red arrow indicates the positive direction of the electric field and the white arrow gives the corresponding direction of the electron transfer. **b**, Temporal profile of the optical field when set to a cosine phase in free space (CEP = 0), as characterized by two-dimensional (2D) spectral shearing interferometry[35]. **c**, The pulse-averaged current induced by the electric field of the light. At the pulse repetition rate of 80 MHz the transfer of one electron per pulse corresponds to a current of 12.8 pA. Results are shown as a function of the free-space amplitude of the electric field of the laser pulse. The current is modulated sinusoidally with a phase φ that is directly related to the far-field CEP of the driving pulse $\varphi = \mathrm{CEP} + \delta$. Because only the relative CEP can be defined experimentally, δ is unknown. The phase of the current variation φ is then defined such that $\varphi = 0$ corresponds to the maximum current, and this reference is used to assign the values in **c**. The line with dots reports the TDDFT result obtained for the phase conditions of the pulse corresponding to the maximum electron transfer.

For the autocorrelation measurements, the current generated at the nanojunction of the circuit is recorded as a function of both the delay between the two pulse replicas and their CEPs. These measurements were performed in air and at room temperature over several minutes. They demonstrate excellent reproducibility of the current signal and high stability of the nanostructure, as indicated by the traces depicted in Fig. 1c, which report the current measured as a function of the optical field amplitude of the single-cycle pulses. This dataset was acquired at different relative CEPs of the driving pulses on a single sample. Note that, because the absolute value of the CEP cannot be defined experimentally, in Fig. 1c we assign the results according to the phase of the sinusoidal modulation of the current, φ. This reference phase is set to zero, $\varphi = \varphi_0 = 0$, for the situation that shows the maximum positive value of the current. In our experiments, the phase shift δ between the absolute value of the far-field CEP and φ is approximately $-\pi/2$, as assessed by the numerical calculations. At perfect temporal overlap between the two pulses (that is, delay $\Delta t = 0$ fs, equivalent to a single pulse), the average optical power amounts to 1.7 mW. This value still corresponds to a minute driving pulse energy of 21 pJ and a free-space peak field of 1 V nm^{-1} at the sample position within the confocal spot of the objective (1.5 µm spot size). Owing to the implementation of smaller gaps and a shorter pulse, we achieve a fourfold increase in the current at a factor of four lower driving energy as compared to our previous results[19], allowing interferometry measurements with unprecedented access to a complex dynamics of electron currents within the gap. The experimental data obtained with a single pulse are reproduced with our TDDFT calculations, allowing retrieval of the amplitude of the electric field in the gap, as well as identification of the absolute value of the CEP that provides the maximum positive current (see Supplementary Information).

Figure 2a presents a full two-dimensional (2D) map of the interferometric autocorrelation that depicts the nonlinear ultrafast current driven by a pulse pair as a function of their relative time delay Δt and CEP. The colour code from blue to red follows the amplitude and direction of the electron transfer. The 2D map of electron transport contains information that goes well beyond standard interferometric autocorrelation measurements based on optical nonlinear signals, where a 1D fringe pattern is acquired as a function of the temporal delay between the pulses. Specifically, it contains one additional degree of freedom on the ordinate: the modulation of the current by varying the CEP encoded in the single-cycle optical fields. Simultaneous access to both the temporal delay and the CEP dependence of electron transport allows unveiling of the complex non-perturbative phenomenon of optical field emission in a nanogap and provides unprecedented details to be exploited in combination with theoretical approaches, as presented in this work. In Fig. 2b the theoretical 2D autocorrelation map shows an excellent qualitative agreement with the experimental one (Fig. 2a). The quantitative comparison between experiment and calculations is presented in Fig. 2c,d which includes a cut of the map at a fixed value of the reference phase φ, and can be conceptually compared to a standard interferometric autocorrelation measurement. The results in Fig. 2e display the dependence of the electron transfer on φ (and thus on the CEP as $\mathrm{CEP} = \varphi - \delta$) at zero time delay, demonstrating full CEP control of the electron currents with a single optical pulse.

From this dataset, it becomes clear that the interferometric autocorrelation originates from a highly non-perturbative process operating on a sub-femtosecond timescale. The interference maxima are significantly shorter than an optical half-cycle of the driving field, featuring a FWHM of ~1 fs. In addition, the autocorrelation signal completely vanishes between the constructive maxima, and the amplitude of the side peaks is strongly reduced with respect to the situation of perfect overlap. Importantly, these findings clearly demonstrate that the electronic transport in the junction is directly connected with the phase of the driving pulse, and that the current dynamics of electronic wavepackets can be controlled on timescales shorter than a half-cycle of the optical field.

To gain microscopic insight into the spatiotemporal electron dynamics induced by the optical field in our nanodevice, we carried out first-principles TDDFT[29] simulations, a very powerful tool in the description of strong field phenomena at metal surfaces[30–32]. Although a full quantum calculation is out of reach for mesoscopic objects like the Au bowties used in the experiments, the main physics can be captured with the reduced system sketched in Fig. 3a. Indeed, for the bowtie used in our experiments, the height $h = 20$ nm is

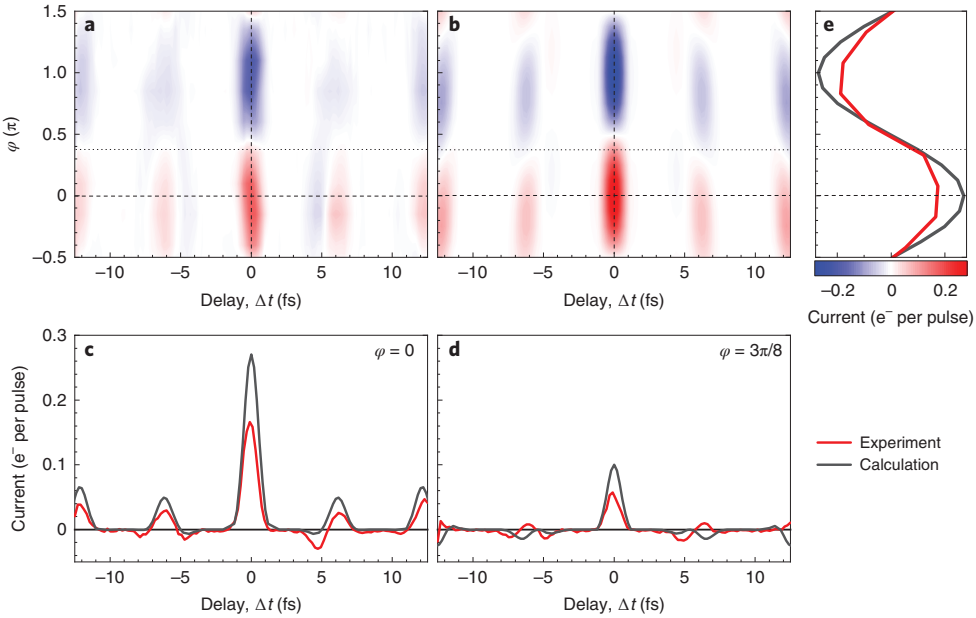

Fig. 2 | Interferometric current autocorrelations dependent on the CEP of the driving pulses. a,**b**, Colour map of the measured (**a**) and calculated (**b**) 2D interferometric autocorrelation acquired as a function of temporal delay Δt and phase φ of the sinusoidal current modulation. **c**, Interferometric autocorrelation (red line) of two identical single-cycle pulses with CEP set to deliver the maximum peak current using the current driven at the nanogap as a nonlinear signal (dashed line in **a**,**b**). The extreme order of nonlinearity is underlined by the absence of signal when the maxima of the field do not overlap at the periodicity of the carrier wavelength. The width of the central peak is ~1 fs. The experimental data are compared with the equivalent trace derived from the calculations (black line). **d**, Same as **c** but acquired at $\varphi = 3\pi/8$ (dotted line in **a**,**b**). **e**, Vertical cut of the 2D colour map at $\Delta t = 0$, which is equivalent to a single pulse illuminating the nanogap. The sinusoidal modulation of the current with phase φ is shown for the experiment (red line) and theory (black line).

larger than the size of the gap and the plasmonic field enhancement strongly confines the region of optical field emission and electron transport to the junction, as follows from the snapshots of the calculated electron current density depicted in Fig. 3b. We then model the plasmonic gap as two infinite parallel Au cylinders described within the free electron (jellium) model. The cylinder radii R_c and their separation distance d_g are adapted to the shape of the antenna as visualized by the scanning electron microscopy (SEM) images ($R_c = 5$ nm and $d_g = 6$ nm). Because the optical response of the nanowire dimer is different from that of the actual bowtie antenna, special care is needed to correctly capture the optical field emission from the metal surfaces facing the gap in the experimental situation. To this end, in the TDDFT calculations, the incident sub-cycle pulse is set such that the time trace of the self-consistent electric field in the gap of the cylinder dimer is equivalent to the one obtained from classical Maxwell's equations for the actual bowtie antenna (for further details see Supplementary Information). The absolute value of the field is calibrated with respect to the experimental dependence of the current on the pulse energy (see the theoretical result in Fig. 1c, plotted as a grey line with dots).

The effect of the plasmonic resonance in the near-field at the gap region of the bowtie nanoantenna can be seen in Fig. 3c. The far-field transient (red line) of a pulse with CEP = 0 in free space becomes distorted within the antenna gap (green line). The field in the junction is enhanced by two orders of magnitude, in line with the data obtained with classical calculations in the literature[11,33]. In addition, a phase shift $\mathrm{CEP}_{gap} - \mathrm{CEP} \approx 0.35\pi$ occurs between the effective phase of the pulse in the near-field of the gap, CEP_{gap}, and that of the far-field transient. This value is obtained from the time dependence of the fields close to $t = 0$ within the central part of the pulse. The plasmon resonance of the nanoantenna results in a few-cycle ringing of the near-field with a characteristic phase shift of $\pi/2$ at large times following the main peak. We show that, in analogy with experiments on multiphoton electron emission from flat metal surfaces[34], an excitation of the antenna plasmon in the present case has a strong effect on the autocorrelation traces.

The enhanced electric field in the junction region drives the optical field emission and thus the electron flow through the gap, as illustrated in Fig. 3d. For an illumination pulse with a CEP = 0 in free space, the antenna resonance shapes the temporal profile of the transient to become almost sine-like in the near-field, with an effective phase $\mathrm{CEP}_{gap} = 0.35\pi$ (Fig. 3c). This effect, combined with the temporal dynamics of the electrons within the gap, leads to two opposite electronic streams, which are produced by the central cycle of the pulse and almost completely cancel each other. The net electron transport through the gap is therefore close to zero in this situation. The entire dynamics is repeated by the following cycles at strongly reduced magnitudes because of the progressive decay of the induced near-field.

The finite propagation time of the photo-emitted electrons through the antenna gap explains an additional offset of the oscillation of the current through the centre of the junction with respect to that of the field in the gap. It is noteworthy, for the present geometry, that the trajectories followed by the electrons differ from what is typically observed in the case of metal tips. For optical field emission from nanotips or individual plasmonic nanoobjects, the fast spatial decay of the electric near-fields reduces the quiver motion of emitted electrons[2,10,11,30]. However, contrary to the case of a single nanoparticle, the electric field in a metallic gap is rather uniform spatially. This fact causes the dynamics of electron transport to be strongly affected by the quiver motion, as illustrated in Fig. 3d. In detail, similar to Fowler–Nordheim emission in strong d.c. fields[30], the early electrons are ejected from the right surface by the strong positive optical field during the first half-period of the pulse with maximum at $t \approx 2$ fs. These electrons appear as a current burst propagating from right to left within the gap. The initial

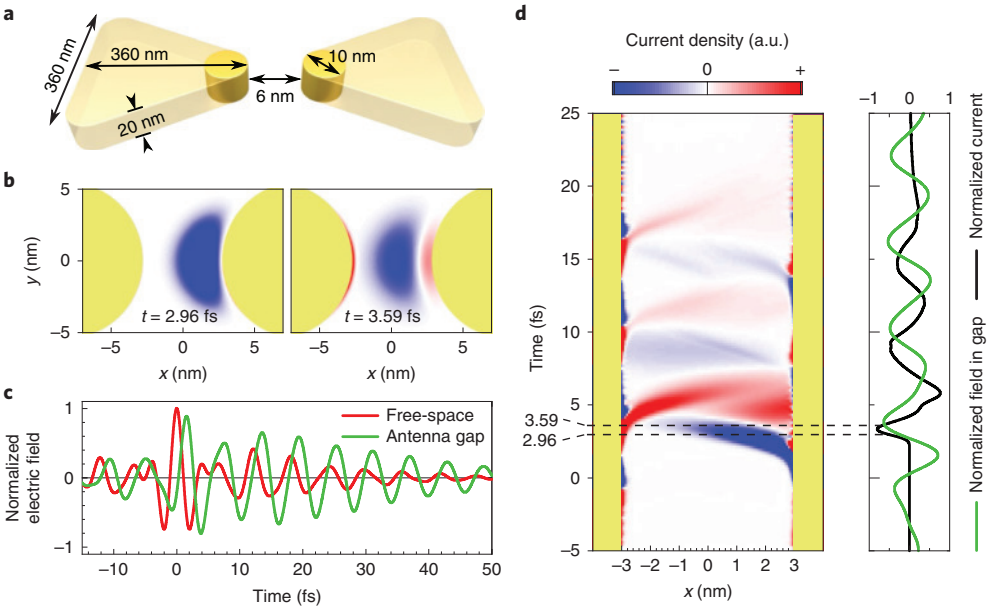

Fig. 3 | Time-dependent calculations of the current density driven by the electric field of the laser pulses. a, Conceptual sketch of the antenna geometry employed for the calculations. The cylinders reproducing the morphology of the antenna apices are used in the TDDFT calculations of the optical field emission, while the plasmonic resonance corresponding to the whole bowtie antenna gap is captured by solving the classical Maxwell's equations. **b**, Snapshots of the electron current density within the gap at two different instants of time, as indicated by dashed lines in **d**. The reference time $t=0$ is set at the maximum of the free-space optical field. **c**, Electric field profile of the far-field illumination of a pulse with CEP = 0 (red) and the corresponding electric field profile calculated in the centre of the gap (green). The fields in the antenna gap are scaled by a factor of 1/100. **d**, Left: colour map of the electron current along the dimer axis, calculated as a function of time for far-field illumination with CEP = 0. Right: corresponding electric field in the gap (green) and integrated electron current across the gap central plane (black). The metal volume is shaded with yellow rectangles.

acceleration is sketched in the left snapshot of Fig. 3b. Because the driving pulse is almost sine-like in the near-field, the polarity of the field changes within the second half-cycle of the pulse, when the electrons are still in the gap. As a result, part of the electrons belonging to the initial burst experiences a complete reversal of sign in the propagation direction (seen as a change of sign of the electron current density from blue-negative to red-positive going through white-zero) approximately at the centre of the junction. This situation is depicted in the right snapshot of Fig. 3b where the red region corresponding to positive current density within the gap appears at positive values of the x coordinate. The positive current density at the negative values of the x coordinate corresponds to the electrons ejected from the left surface by the strong optical negative field during the second half-period of the pulse with an extremum value at $t \approx 4$ fs (see also Fig. 3d). The quiver motion of the ejected electrons is further illustrated with classical electron trajectories in Supplementary Fig. 9, which provides a classical analogue to the results of the TDDFT calculations in Fig. 3d.

In the present case, the amplitude of the quiver motion $X_Q = E_g/\omega^2$ (E_g is the maximum value of the field in the gap and ω is the central frequency of the pulse; all values are expressed in atomic units) is such that the electron excursion $2X_Q$ is essentially smaller than the size of the gap, thus enabling coherent motion of the ejected electrons. This aspect has a direct consequence for the CEP conditions for maximum electron transport to occur, because a significant number of the electrons does not cross the junction directly, but experiences a quiver motion with several reversals of the direction of propagation before crossing the gap (examples of the classical electron trajectories are provided in the Supplementary Information). The dynamics of the electron currents is further complicated by the presence of the small fraction of electrons rescattered from the parent tip and from the opposite tip across the junction. Nevertheless, the optimal CEP provides a drift velocity such that the electrons emitted at the central part of the pulse cross the junction. In fact, we calculate that the maximum electron transfer is reached for CEP = 0.49π of the far-field transient, resulting in the effective phase $\mathrm{CEP}_{\mathrm{gap}} = 0.84\pi$ of the central part of the pulse in the near-field of an antenna gap (Supplementary Fig. 11). Therefore, the match between the measured and calculated sinusoidal modulation of the current at delay $\Delta t = 0$ fs in Fig. 2e allows us to unambiguously determine the absolute value of the free-space CEP in the experiment. Along with the possibility to determine the CEP of the experimental transient, the remarkable agreement between the modelled and experimental results also reveals the role of the plasmon mode of the nanoantenna. It follows from our calculations that the secondary maxima in the experimental autocorrelation plot in Fig. 2c emerge owing to the overlap of the strong fields at the central part of the second replica with the resonantly enhanced near-fields at large time delays following the first pulse. In fact, in the ideal case of a flat antenna response, the autocorrelation signal obtained with TDDFT is zero at every time delay except for the central cycle.

In both the measured and calculated data, the CEP dependence of the secondary maxima is slightly phase-shifted with respect to the main peak. This result stems from the following: (1) the non-Gaussian, asymmetric profile of the driving pulse for which the slowly varying envelope approximation is not valid (that is, the carrier cannot be considered monochromatic) and thus may be affected by some residual chirp and (2) the resonance effect of the plasmonic antenna that shapes the field within the gap and defines the quiver motion of electrons emitted at different instants of time. This aspect becomes even clearer in the interferometric autocorrelation plotted in Fig. 2d. The experimental data (red lines) and theoretical results (black lines) correspond to the constant phase $\varphi = 3\pi/8$ cut of the autocorrelation maps of Fig. 2a,b. The signs of the secondary maxima are reversed with respect to those of the main peak at $\Delta t = 0$. Altogether, the high nonlinearity of the optical field emission allows

for using our device as a sensitive probe of the dynamics of the near-fields in plasmonic gaps.

In conclusion, the interferometric autocorrelation measurements performed with single-cycle pulses that coherently drive electric currents at the gap of a single nanodevice show that it is possible to achieve an extremely nonlinear regime, even at minute pJ pulse energies. Along with optical field emission, the understanding of the complex dynamics of the field-driven transport investigated with extreme temporal resolution demonstrates that we can model and control the transfer of individual electrons between two metallic nanocontacts and access the evolution of plasmonic fields in the nanogap on a sub-cycle timescale. Therefore, tracing and dissecting an ultrashort photocurrent in a plasmonic nanogap is found to be crucial for the proper design of integrated plasmonic and optoelectronic devices that operate in the single-electron regime at optical frequencies. In addition, the theoretical developments and fundamental understanding of electronic dynamics driven at the nanoscale by optical fields, as achieved in this work, will allow us to target future experiments where electron transport is confined to both atomic time and length scales.

References

1. Krauss, G. et al. Synthesis of a single cycle of light with compact erbium-doped fibre technology. *Nat. Photon.* **4**, 33–36 (2010).
2. Herink, G., Solli, D., Gulde, M. & Ropers, C. Field-driven photoemission from nanostructures quenches the quiver motion. *Nature* **483**, 190–193 (2012).
3. Dombi, P., Krausz, F. & Farkas, G. Ultrafast dynamics and carrier-envelope phase sensitivity of multiphoton photoemission from metal surfaces. *J. Mod. Opt.* **53**, 163–172 (2006).
4. Krüger, M., Schenk, M. & Hommelhoff, P. Attosecond control of electrons emitted from a nanoscale metal tip. *Nature* **475**, 78–81 (2011).
5. Schiffrin, A. et al. Optical-field-induced current in dielectrics. *Nature* **493**, 70–74 (2012).
6. Piglosiewicz, B. et al. Carrier-envelope phase effects on the strong-field photoemission of electrons from metallic nanostructures. *Nat. Photon.* **8**, 37–42 (2013).
7. Paasch-Colberg, T. et al. Solid-state light-phase detector. *Nat. Photon.* **8**, 214–218 (2014).
8. Cocker, T. L. et al. An ultrafast terahertz scanning tunneling microscope. *Nat. Photon.* **7**, 620–623 (2013).
9. Gao, C.-Z. et al. Strong-field effects in the photoemission spectrum of the C_{60} fullerene. *Phys. Rev. A* **93**, 022506 (2016).
10. Echternkamp, K. E. et al. Strong-field photoemission in nanotip near-fields: from quiver to sub-cycle electron dynamics. *Appl. Phys. B* **122**, 80 (2016).
11. Dombi, P. et al. Ultrafast strong-field photoemission from plasmonic nanoparticles. *Nano Lett.* **13**, 674–678 (2013).
12. Cocker, T. L., Peller, D., Yu, P., Repp, J. & Huber, R. Tracking the ultrafast motion of a single molecule by femtosecond orbital imaging. *Nature* **539**, 263–267 (2016).
13. Ahn, B. et al. Attosecond-controlled photoemission from metal nanowire tips in the few-electron regime. *APL Photon.* **2**, 036104 (2017).
14. Vogelsang, J., Hergert, G., Wang, D., Groß, P. & Lienau, C. Observing charge separation in nanoantennas via ultrafast point-projection electron microscopy. *Light Sci. Appl.* **7**, 4–11 (2018).
15. Jelic, V. et al. Ultrafast terahertz control of extreme tunnel currents through single atoms on a silicon surface. *Nat. Phys.* **13**, 591–598 (2017).
16. Yoshioka, K. et al. Tailoring single-cycle near field in a tunnel junction with carrier-envelope phase-controlled terahertz electric fields. *Nano Lett.* **18**, 5198–5204 (2018).
17. Yoshioka, K., Katayama, I., Minami, Y., Kitajima, M. & Yoshida, S. Real-space coherent manipulation of electrons in a single tunnel junction by single-cycle terahertz electric fields. *Nat. Photon.* **10**, 762–765 (2016).
18. Rácz, P. et al. Measurement of nanoplasmonic field enhancement with ultrafast photoemission. *Nano Lett.* **17**, 1181–1186 (2017).
19. Rybka, T. et al. Sub-cycle optical phase control of nanotunnelling in the single-electron regime. *Nat. Photon.* **10**, 667–670 (2016).
20. Putnam, W. P., Hobbs, R. G., Keathley, P. D., Berggren, K. K. & Kärtner, F. X. Optical-field-controlled photoemission from plasmonic nanoparticles. *Nat. Phys.* **13**, 335–339 (2017).
21. Savage, K. et al. Revealing the quantum regime in tunnelling plasmonics. *Nature* **491**, 574–577 (2012).
22. Esteban, R. et al. A classical treatment of optical tunneling in plasmonic gaps: extending the quantum corrected model to practical situations. *Faraday Discuss.* **178**, 151–183 (2015).
23. Wan, Y., Wubs, M. & Mortensen, N. A. Projected dipole model for quantum plasmonics. *Phys. Rev. Lett.* **115**, 137403 (2015).
24. Zhu, W. et al. Quantum mechanical effects in plasmonic structures with subnanometre gaps. *Nat. Commun.* **7**, 11495 (2016).
25. Hanke, T. et al. Tailoring spatiotemporal light confinement in single plasmonic nanoantennas. *Nano Lett.* **12**, 992–996 (2012).
26. Aguirregabiria, G. et al. Dynamics of electron-emission currents in plasmonic gaps induced by strong fields. *Faraday Discuss.* **214**, 147–157 (2019).
27. Brida, D., Krauss, G., Sell, A. & Leitenstorfer, A. Ultrabroadband Er:fiber lasers. *Laser Photon. Rev.* **8**, 409–428 (2014).
28. Krauss, G. et al. All-passive phase locking of a compact Er:fiber laser system. *Opt. Lett.* **36**, 540–542 (2011).
29. Marques, M. A. L. & Gross, E. K. U. Time-dependent density functional theory. *Annu. Rev. Phys. Chem.* **55**, 427–455 (2004).
30. Krüger, M., Lemell, C., Wachter, G., Burgdörfer, J. & Hommelhoff, P. Attosecond physics phenomena at nanometric tips. *J. Phys. B* **51**, 172001 (2018).
31. Lemell, C., Tong, X., Krausz, F. & Burgdörfer, J. Electron emission from metal surfaces by ultrashort pulses: determination of the carrier-envelope phase. *Phys. Rev. Lett.* **90**, 076403 (2003).
32. Wachter, G. et al. Electron rescattering at metal nanotips induced by ultrashort laser pulses. *Phys. Rev. B* **86**, 035402 (2012).
33. Schuck, P. J., Fromm, D. P., Sundaramurthy, A., Kino, G. S. & Moerner, W. E. Improving the mismatch between light and nanoscale objects with gold bowtie nanoantennas. *Phys. Rev. Lett.* **94**, 017402 (2005).
34. Dombi, P. et al. Observation of few-cycle, strong-field phenomena in surface plasmon fields. *Opt. Express* **23**, 24206–24212 (2010).
35. Birge, J. R., Ell, R. & Kärtner, F. X. Two-dimensional spectral shearing interferometry for few-cycle pulse characterization. *Opt. Lett.* **31**, 2063–2065 (2006).

Methods

Source of control transients. The elements of the Er:fibre laser system providing the ultrashort optical control pulses exploited in our experiment are described in detail in ref. [16]. Here, single-cycle near-infrared transients that are passively phase-locked were generated at a repetition rate as high as 80 MHz by combining super-octave-spanning coherent synthesis with elimination of the CEP slip via difference frequency mixing and re-amplification. The present implementation of the system is even superior to our earlier results in terms of pulse duration[1]. The laser system also offers precise CEP control by placing a pair of fused-silica wedges before the last Er:fibre amplifier and final compression. The minimum duration is achieved by independent soliton and dispersive wave compression (with a three-prism set-up) before coherent combination of the two spectral components produced by a highly nonlinear fibre.

For full temporal reconstruction of the pulse, we performed a direct characterization using 2D spectral shearing interferometry. This method allows direct reconstruction of the electric field profile, that is, the amplitude and phase of the electromagnetic wave. It is particularly suited for super-octave-spanning spectra. By fine-tuning the dispersion via an SF10 prism pair, we obtained an almost flat phase over the entire spectrum. This result corresponds to a pulse duration of 4.2 fs and one optical cycle at the central wavelength of 1,250 nm. The complete characterization is provided in the Supplementary Information.

Antenna fabrication and characterization. The nanostructured electronic circuit equipped with a plasmonic antenna was fabricated by electron-beam lithography. A fused-silica window was spincoated with a 60 nm layer of PMMA (950k) resist. Heating the substrate above 100 °C before deposition evaporated residual water on the surface. An 8 nm-thick thermally evaporated layer of aluminium provided the necessary electric conduction to avoid distortion due to charging effects during exposure. The structures were written with an areal dose of 400 pC cm^{-2} at 10 kV. Subsequently, the aluminium layer was removed in a bath of sodium hydroxide followed by a rinse in deionized water. Development of the resist was carried out in a mixture of methyl isobutyl ketone (MIBK), methyl ethyl ketone (MEK) and isopropanol (IPA) in a volume ratio of 100:6:300. The gold nanostructures were patterned in a subsequent evaporation process in which 18 nm of gold was evaporated on top of a 2 nm chromium adhesion layer, followed by a liftoff process in a bath of acetone. The electronic interface between the nanostructures and the detection electronics was provided by a custom-made circuit board into which the fused-silica substrates were integrated and connected by wire bonding.

TDDFT. The dynamics of the electron density induced by a laser pulse were obtained by solving the time-dependent Kohn–Sham (KS) equations[29] (where $\mathbf{r} = (x,y,z)$ is the electron position vector):

$$i\partial_t \psi_k(\mathbf{r},t) = \{T + V_{\mathrm{Au}} + V_{\mathrm{xc}}(n) + V_{\mathrm{H}}(n) + V^{\mathrm{ext}}(t)\}\psi_k(\mathbf{r},t) \qquad (1)$$

This equation describes the evolution of the Kohn–Sham (KS) orbitals ψ_k under the action of an external potential V^{ext}. The incident laser pulse is treated within the dipole approximation. In the Coulomb gauge the external potential is given by $V^{\mathrm{ext}} = E^{\mathrm{ext}}(t)x$, where $E^{\mathrm{ext}}(t)$ describes the external field, and the dimer x axis is defined in Fig. 3a. In equation (1), T is the kinetic energy operator, V_{Au} describes the electron interaction with atomic cores, $V_{\mathrm{xc}}(n)$ is the exchange-correlation potential treated within the adiabatic local density approximation[29] with the exchange-correlation kernel of Gunnarsson and Lundqvist[36] and $V_{\mathrm{H}}(n)$ is the Hartree potential. The time-dependent electronic density of the system is given by $n(\mathbf{r},t) = \sum_{k=\mathrm{occ}} |\psi_k(\mathbf{r},t)|^2$ where the summation runs over the occupied KS orbitals. The initial conditions $\psi_k^0(\mathbf{r})$ are given by the KS orbitals of the ground-state system, obtained from the ground-state DFT calculation:

$$\underbrace{\{T + V_{\mathrm{Au}} + V_{\mathrm{xc}}(n_0) + V_{\mathrm{H}}(n_0)\}}_{H_0}\psi_k^0(\mathbf{r}) = E_k\psi_k^0(\mathbf{r}) \qquad (2)$$

where the Hamiltonian H_0 depends on the ground-state density via the exchange-correlation and Hartree potentials. Consistent with TDDFT, the exchange-correlation kernel of Gunnarsson and Lundqvist is used for $V_{\mathrm{xc}}(n_0)$, where $n_0(\mathbf{r}) = \sum_{k=\mathrm{occ}} |\psi_k^0(\mathbf{r},t)|^2$.

Considering the dimer of two infinite cylindrical nanowires with $d_g = 6$ nm as a reduced model mimicking the bowtie antenna gap brings the system within reach of quantum calculations if the free electron (jellium) description of the metal[37] is used. Within the jellium model (JM) the ionic cores at the gold lattice sites are replaced by the uniform positive background charge of density $n_+ = \left[\frac{4\pi}{3} r_s^3\right]^{-1}$. We use $r_s = 3a_0$, characteristic for the valence electron density of gold ($a_0 = 0.053$ nm is the Bohr radius). At the price of losing atomistic details, this approach allows us to follow the dynamics of the valence electrons of the metal involved in the screening, optical field emission and electron transport[9,30–32,38]. Note also that the JM has been successfully employed in the context of plasmonics, allowing theoretical prediction of quantum effects that were later confirmed experimentally[24].

The reduced model of the cylindrical nanowire dimer reproduces well the optical field electron emission and electron transport in the gap of the realistic bowtie antenna. However, the exact description of the electric field induced in the gap region, including the macroscopic effect of the actual triangular dimer, is of paramount importance for capturing the details of electron emission and transport. To this end, we solve the classical Maxwell's equations, and we calculate the field in the gap $E_g(t)$ for the actual silica-supported bowtie nanoantenna subjected to the experimental incident pulse. (As a reference, we use the field $E_g(t)$ in the centre of the junction.) In the TDDFT calculations, $E^{\mathrm{ext}}(t)$ is then set in such a way that the self-consistent field in the gap equals $E_g(t)$. The absolute value of the electric field strength used in the TDDFT calculations has been set such that the experimental data obtained with $\Delta t = 0$ and the CEP corresponding to the maximum electron transfer are reproduced as shown in Fig. 1. For a transfer of 0.2 electrons per pulse, we found that the field in the gap is of the order of 10 V nm^{-1} and we used this value for all TDDFT calculations. This fact implies an 11-fold enhancement of the free-space electric field, which is significantly lower than the theoretical estimate based on the solution of the classical Maxwell's equations. However, it has to be considered as an effective value accounting for the experimental uncertainties, as well as for the model geometry used in the TDDFT study and possible nonlinear effects leading to a strong reduction of the field enhancement as compared to the predictions of classical linear theory[39].

Given the time-dependent solutions of the KS equations $\psi_k(\mathbf{r},t)$, one can obtain the time-dependent probability current density

$$\mathbf{j}(\mathbf{r},t) = -\tfrac{i}{2}\sum_{k=\mathrm{occ}} \{\psi_k^*(\mathbf{r},t)\nabla\psi_k(\mathbf{r},t) - \psi_k(\mathbf{r},t)\nabla\psi_k^*(\mathbf{r},t)\} \qquad (3)$$

and the total electron current per unit height through the centre of the gap ($\hat{\mathbf{e}}_x$ is the unit-length vector along the x axis)

$$I(t) = \int \hat{\mathbf{e}}_x \mathbf{j}(\mathbf{r},t)|_{x=0}\,\mathrm{d}y \qquad (4)$$

The theoretical prediction for the number of electrons transferred across the gap of the bowtie nanoantenna is then given by $N = h\int_{t_0}^{T} I(t)\mathrm{d}t$, where $h = 20$ nm is the height of the nanoantenna. The final propagation time is taken to be large enough that the electric field becomes small and the electron transfer stops.

The TDDFT results presented in Fig. 2 could be reproduced with the use of a classical simple man's model[30] (see Supplementary Information) assuming a flat gap geometry, which is a simpler and tackleable geometry than that used in our TDDFT calculations. Thus, the calculated 2D interferometric autocorrelation stems from robust underlying physical phenomena such as optical field emission from the metal surfaces and the subsequent electron motion in the time-varying field. Because the time evolution of the fields in the junction used in the theoretical description takes into account plasmonic effects, we conjecture that the TDDFT results presented in this work are qualitatively robust with respect to small variations of the system geometry and with respect to the JM description of gold.

References

36. Gunnarsson, O. & Lundqvist, B. I. Exchange and correlation in atoms, molecules, and solids by the spin-density-functional formalism. *Phys. Rev. B* **13**, 4274–4298 (1976).
37. Lang, N. D. & Kohn, W. Theory of metal surfaces: work function. *Phys. Rev. B* **3**, 1215–1223 (1971).
38. Nguyen, H. S., Bandrauk, A. D. & Ullrich, C. A. Asymmetry of above-threshold ionization of metal clusters in two-color laser fields: a time-dependent density-functional study. *Phys. Rev. A* **69**, 063415 (2004).
39. Zuloaga, J., Prodan, E. & Nordlander, P. Quantum plasmonics: optical properties and tunability of metallic nanorods. *ACS Nano* **4**, 5269–5276 (2010).

Acknowledgements

D.B. and A.L. acknowledge support of the Deutsche Forschungsgemeinschaft through the Emmy Noether programme (BR 5030/1-1) and the collaborative research centre SFB 767. D.B. acknowledges support from the European Research Council through grant no. 819871 (UpTEMPO). G.A. acknowledges project PI2017-30 of the Departmento de Educación, Política Lingüística y Cultura de la Basque Government, and G.A. and J.A. acknowledge funding from project FIS2016-80174-P of the Spanish Ministry of Science, Innovation and Universities MICINN, as well as grant IT1164-19 for consolidated university groups of the Basque Government.

Author contributions

J.A., A.G.B., A.L. and D.B. conceived the project. A.L. and D.B. supervised the experimental activity. M.L., F.R. and T.R. fabricated the nanostructures, developed the set-up and performed the measurements. J.A. and A.G.B. coordinated the theoretical modelling. G.A., D.C.M. and A.G.B. developed the theory simulations. All authors contributed to the discussion of the data and to writing the manuscript.

Competing interests

The authors declare no competing interests.